Turbulent Energy Budget Analysis Based on Coherent Wind Lidar Observations

Jinhong Xian[1,2], Zongxu Qiu[2], Hongyan Luo[2], Yuanyuan Hu[2], Xiaoling Lin[2], Chao Lu[2], Yan Yang[2], Honglong Yang[2], Ning Zhang[1,3]

[1] School of Atmospheric Sciences, Nanjing University, Nanjing 210023, China
[2] Shenzhen National Climate Observatory, Meteorological Bureau of Shenzhen Municipality, Shenzhen 518040, China
[3] Key Laboratory of Urban Meteorology, China Meteorological Administration, Beijing, 100089, China

Correspondence to: Honglong Yang (yanghonglong@weather.sz.gov.cn); Ning Zhang (ningzhang@nju.edu.cn)

Abstract. The turbulent kinetic energy (TKE) budget terms, which collectively are a key physical quantity for describing the generation and dissipation processes of turbulence, are crucial for revealing the essence and characteristics of turbulence. Due to limitations in current observational methods, the generation and dissipation mechanisms of atmospheric turbulent energy are mainly based on ground or tower-based observations, and studies on the budget terms of TKE of vertical structures are lacking. We propose a new method for detecting TKE budget terms based on coherent wind lidar, and compare it with data obtained with a three-dimensional ultrasonic anemometer. The results indicate that the error of the buoyancy generation term estimated by the wind lidar is relatively small, less than 0.00014 m^2/s^3, which verifies the accuracy and reliability of our method. We explore the generation and dissipation mechanisms of turbulence under different weather conditions, and find that the buoyancy generation term plays a role in dissipating TKE under low cloud and light rain conditions. During the day, turbulent transport and the dissipation rate are the main dissipation terms, while buoyancy generation is the main dissipation term at night. The results show that the proposed method can accurately capture the vertical distribution of TKE, dissipation rate, shear generation, turbulent transport, and buoyancy generation terms in the boundary layer, and can comprehensively reflect the influence of each budget term on the vertical structure of turbulent energy. This research provides a new perspective and method for studies of atmospheric turbulence, which can be further applied to fine observations of the vertical structure and dynamics of turbulence.

1 Introduction

Turbulence is an important phenomenon in atmospheric thermodynamics and dynamics. Its generation and dissipation mechanisms are of great significance for understanding atmospheric motion, predicting weather changes, and evaluating wind energy resources (Heilman et al., 2018; Stull, 1988; Byzova et al., 1989; Kaimal et al., 1976). The turbulent kinetic energy (TKE) budget terms, which are key physical quantities for describing the generation and dissipation processes of turbulence, are crucial for revealing the essence and characteristics of turbulence (Stull, 1988).

Boundary layer parameterization schemes can be used to predict the vertical distribution of TKE and its budget terms by simulating turbulent processes, thereby allowing the impact of different physical

processes on TKE changes to be analyzed (Nilsson et al., 2016b; Elguernaoui et al., 2023). Simulating turbulence typically requires the use of direct numerical simulations or large eddy simulations. These methods usually demand substantial computational resources (Elguernaoui et al., 2023). The boundary layer parameterization schemes currently used, such as the Yonsei University (YSU) scheme, Mellor–Yamada–Janjic (MYJ) scheme, Mellor–Yamada–Nakanishi–Niino Level 2.5 (MYNN2) scheme, and Asymmetric Convective Model version 2 (ACM2), make certain assumptions and simplifications when simulating turbulent processes, which inevitably lead to inaccurate predictions of TKE (Hariprasad et al., 2014). For example, the YSU scheme tends to overestimate or underestimate mechanical turbulence, turbulent mixing intensity, or entrainment processes, thereby affecting the prediction results of TKE (Hong et al., 2006). The MYJ scheme underestimates the actual turbulence intensity when the TKE is predicted during the day, causing the predicted values to be smaller than the actual observed values, especially under strong convection or complex terrain conditions (Janjic, 1994). For the MYNN2 parameterization scheme, the prediction of TKE under complex weather conditions is not accurate enough. Therefore, some authors sought to enhance these parameterization schemes through optimization (Hariprasad et al., 2014; Xie et al., 2013). Nilsson et al. proposed a simple model to describe the evolution of TKE and its budget under shear convective atmospheric conditions (Nilsson et al., 2016b). The core of this model is that the variation of TKE is determined by four budget terms (turbulence dissipation rate, buoyancy generation, shear generation, and vertical transmission of TKE), and only three measurable input parameters (near surface buoyancy flux, boundary layer depth, and the wind speed at a certain height of the surface layer) are needed to predict the vertical distribution of TKE and its budget terms. However, in the atmospheric boundary layer, the generation and dissipation of turbulent energy are complex physical processes that are influenced by various factors, including changes in surface heat flux, atmospheric stability, and topography(Guo et al., 2021). Especially for turbulence in the free convection boundary layer, its dynamic characteristics are quite complex, and there are significant differences between the results of models and measurement. Indeed, high-resolution observations are needed to reveal its inherent mechanisms (Goger et al., 2018; Lobocki, 2017; Solanki et al., 2022).

In previous studies, observations of the energy generation and dissipation mechanisms of atmospheric turbulence were mainly based on near-ground or tower-based observations (Baas et al., 2018; Babic and Rotach, 2018; Barman et al., 2019; Bodini et al., 2018; Caughey and Wyngaard, 1979; Hang et al., 2020; Jensen et al., 2017; Lobocki, 2017; Tong et al., 2022; Yus-Diez et al., 2019; Nilsson et al., 2016a). Nilsson et al. (2016a) used near surface measurement data from a small tower to conduct a detailed analysis of various terms in the TKE budget, including the trend, buoyancy generation, dissipation, and transport terms, revealing various differences in the surface layer dynamics of TKE and its attenuation at different periods of the day. Canut et al. successfully measured turbulence flux and variance in the atmospheric boundary layer using an acoustic anemometer bound to a tethered balloon, and conducted an in-depth analysis of the variation patterns of these parameters (Canut et al., 2016). Li et al. analyzed changes in the boundary layer structure, turbulence intensity, and flux of the sea breeze front (SBF) using observational data obtained from two meteorological towers (Tianjin Meteorological Tower and Beijing Meteorological Tower) (Li et al., 2023). Their study indicated that the passage of the

SBF leads to an increase in mechanical turbulence, manifested by an increase in friction velocity and TKE, and the shear generation term in the TKE budget equation underwent a more significant increase than the buoyancy generation term. Pozzobon et al. collected turbulence data at four different height levels (3, 6, 14, and 30 m) over a period of 10 months at a 30 m tower, and studied the TKE budget under convective daytime conditions and stable nighttime conditions (Pozzobon et al., 2023). Their results indicated that during the day, the TKE budget was mainly dominated by shear and buoyancy generation, while dissipation was the main dissipation mechanism. At night, the TKE budget was mainly generated by shear, while the buoyancy generation term played a dissipation role.

However, tower-based observations have certain drawbacks, such as a limited detection range and high construction and maintenance costs, and previous research mainly focused on the near-ground TKE budget and its variational patterns. As such, there is still a lack of research on the various budget terms of TKE for vertical structures. With the rapid development of meteorological observation technology, laser wind measurement technology has gradually become an important tool in the field of wind field observations due to its high precision, high resolution, and wide detection range. Especially in the study of atmospheric turbulence, the application of coherent wind lidar has demonstrated its unique advantages (Banakh et al., 2021; Banakh, 2013; Xian et al., 2023; Rios and Ramamurthy, 2023). In our previous studies, the direct acquisition of atmospheric turbulence parameters was achieved based on wind lidar (Xian et al., 2024c; Xian et al., 2024b). On this basis, we developed a new detection method for TKE budget terms to study the generation and dissipation mechanism of turbulent energy in the vertical direction of the boundary layer, the results of which are presented in this study.

The remainder of this paper is organized as follows. In Section 2, we introduce the instrument and data quality control methods. In Section 3, we introduce methods for obtaining various TKE budget terms based on wind lidar data and compare them with the data obtained with a three-dimensional ultrasonic anemometer to verify the accuracy of the proposed method. In Section 4, we use the measured data to analyze the spatiotemporal variation characteristics of the TKE budget term in classical cases, and explore the variational patterns of each budget term under different weather conditions. The main conclusions of this study are presented in Section 5.

2 Instruments and Data Quality Control

The Shiyan Observation Base (113.90586 °E, 22.65562 °N) is located in the remote suburbs of Shenzhen, with no large obstacles (such as high-rise buildings) around it. One to two km northeast of the base is farmland, while the terrain to the south and northwest is generally flat, almost completely covered by forests and lakes, as shown in Figure 1(a). The base has the highest meteorological gradient observation tower in Asia, which is 356 m high. Due to its advantageous geographical location and the absence of obstacles around it, the wind field and temperature data obtained by the three-dimensional ultrasonic anemometer and thermometer on the gradient observation tower can represent the environmental characteristics of the region (Zhou et al., 2023). Ultrasonic anemometers (CSAT3, Campbell Scientific, Utah, USA) capable of simultaneously observing the wind speed and temperature in three dimensions were installed on the tower at heights of 160 m and 320 m. The observation frequency of the ultrasonic anemometer is 10 Hz, with a wind speed accuracy of 0.1 m/s and a

temperature accuracy of 0.002 K. A coherent wind lidar was installed under the gradient observation tower, as shown in Figure 1(b). The wind lidar (DSL-W, Darsunlaser Technology Co., Ltd., Shenzhen, China) has a detection blind zone of only 30 m, with a maximum detection altitude of 3 km and a vertical resolution of 30 m. The time resolution is 5 s, which means the observation frequency is 0.2 Hz. Specific performance indicators of the laser anemometer and the three-dimensional ultrasonic anemometer are shown in Table 1.

The following quality control steps were taken for the wind speed and temperature data obtained with the three-dimensional ultrasonic anemometer.

(1) *Calculation of statistical parameters*. Calculate the average and standard deviation of the observed values using 30 min intervals.

(2) *Outlier identification and handling*. Any observed value that deviates more than three times the standard deviation from the mean is marked as outlier data and designated as a missing value. This is based on the commonly used "triple standard deviation principle" in statistics, which means that the probability of data points falling outside the mean plus or minus three standard deviations is very small (close to zero), and therefore, these points are considered outliers. This process is repeated three times to ensure accurate identification and handling of outliers.

(3) *Data loss rate*. Within 30 min, if the number of lost measurements exceeds 20%, the data for that period are discarded.

(4) *Coordinate axis correction*. To eliminate wind speed errors caused by installation tilt errors of the ultrasonic anemometers, a dual rotation method is used to correct the coordinate axis, ensuring the accuracy and reliability of the wind speed data (Zhou et al., 2023).

Next, we undertook the following quality control steps for the wind lidar data.

(1) *Calculation of statistical parameters*. Calculate the average and standard deviation of the wind speed and direction every 30 minutes.

(2) *Outlier removal*. We identify outliers and eliminate data points that deviate from the mean by more than three standard deviations, following the same method as described above.

(3) *Integrity of the profile data*. For a single wind speed profile data set, if more than 20% of data points below 500 m are lost, the entire profile is discarded to ensure data integrity and reliability.

Turbulence stationarity test. When studying the characteristics of atmospheric boundary layer turbulence, methods such as correlation analysis and spectral analysis are usually employed. These analysis methods are usually based on the premise that atmospheric turbulence fluctuations have relatively stable statistical characteristics over a certain period, which is called "stationarity" (Massman, 2006) . The requirement for stationarity is that the main statistical characteristics of turbulence, such as variance, should remain stable during the selected observation period. In short, this means that throughout the entire observation period, the average of the overall variance should be close to the average of the variances in each shorter period (Massman, 2006). In this study, a strategy is adopted to compare the average variance within a 30 min observation period with the average variance of six 5 min

samples within the same period. By calculating the deviation between these two and setting a threshold (such as less than 0.3), we filter the data to ensure the reliability of the subsequent analysis.

Overall, these data quality control processes aim to ensure the accuracy, completeness, and reliability of the data through statistical methods and physical corrections. This is crucial for accurate inference of the turbulence parameters, as their values largely depend on the accuracy of the wind speed measurements and the assumption of stationarity.
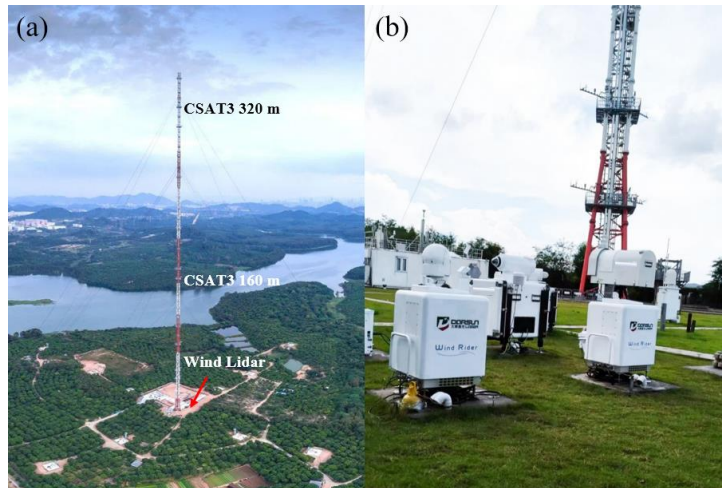
Figure 1. The three-dimensional ultrasonic wind and temperature sensors installed at the meteorological gradient observation tower (a) and the wind lidar used to make wind measurements, located under the tower (b).

Table 1. Performance parameters of the ultrasonic anemometer and wind lidar instrument

	Metric	Technical Performance Requirements
Ultrasonic anemometer	Observational frequency	10 Hz
	Resolution of the wind speed	≤0.1 m/s
	Resolution of the wind direction	≤1°
	Range of wind speed measurements	0–40 m/s
	Temperature accuracy	≤0.002 K
Wind Lidar	Minimum detection altitude	≤30 m
	Maximum detection altitude	3 km
	Distance resolution	30 m
	Observational frequency of the wind profile	0.2 Hz
	Resolution of the wind speed	≤0.1 m/s
	Resolution of the wind direction	≤1°
	Range of wind speed measurements	0–60 m/s
	Range of wind direction measurements	0°– 360°

To verify the accuracy of the data that passed the above quality control processes, a comparison was made between the three wind speed components (u, v, w) measured by the ultrasonic anemometer and the wind lidar, as shown in Figure 2. It can be seen from the figure that the two data sets have relatively high consistency, which lays a solid foundation for the subsequent analysis.
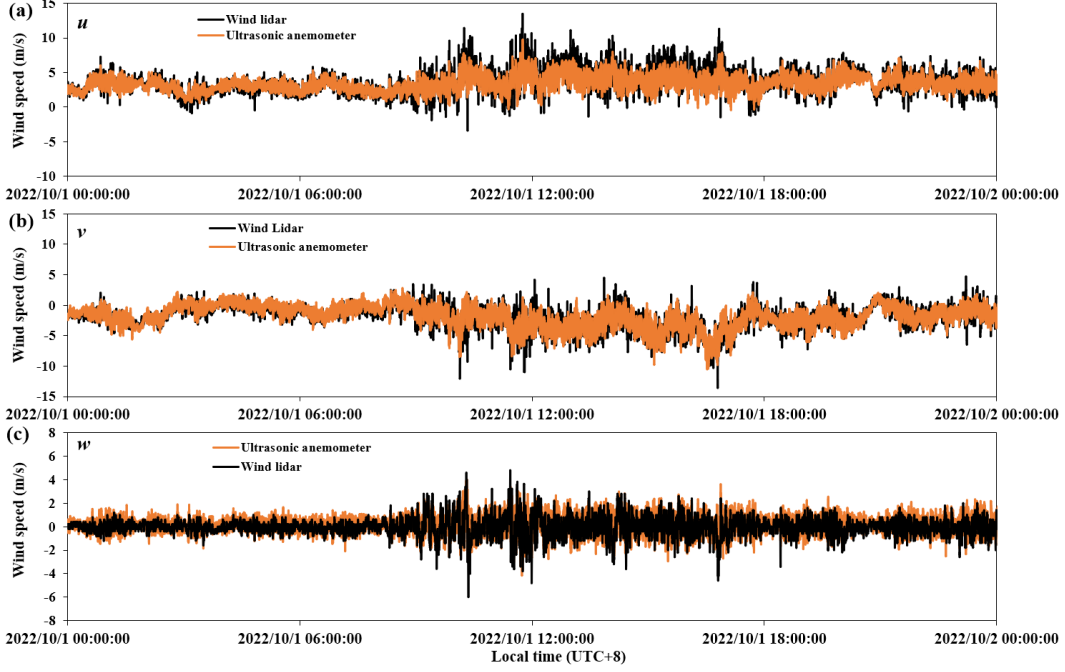
Figure 2. Comparison of the three wind speed components measured by the ultrasonic anemometer (orange) and wind lidar (black).

3 Methodology

3.1 Theory

The TKE equation can be expressed as (Stull, 1988; Nilsson et al., 2016a)

$$\underbrace{\frac{\partial E}{\partial t}}_{E_t} = \underbrace{-\overline{u'w'}\frac{\partial u}{\partial z} - \overline{v'w'}\frac{\partial v}{\partial z}}_{S} + \underbrace{\frac{g}{\theta_m}\overline{w'\theta'}}_{B} - \underbrace{\frac{\partial \overline{w'E'}}{\partial z}}_{T_t} - \underbrace{\frac{\partial \overline{w'p'/\rho_0}}{\partial z}}_{T_p} - \underbrace{\varepsilon}_{D}, \tag{1}$$

where E represents TKE (m^2/s^2), t is the time (s), and u', v', and w' are the fluctuation values of the three-dimensional wind speed components u, v, and w, respectively, which vary with height z; g is gravitational acceleration, θ_m is the average absolute temperature, θ' is the fluctuation value of the absolute temperature θ, ρ_0 is the air density, P' is the fluctuation value of the air pressure P, and ε is the average dissipation rate of TKE. On the left side of the equation is the tendency term (Et), while on the right side are the budget terms for shear generation (S), dissipation rate (D), turbulent transport (T_t), pressure transport (T_P), and buoyancy generation (B). Next, we will introduce how to obtain the above budget terms based on wind lidar data.

3.2 Determination of Turbulent Kinetic Energy and the Tendency Term

TKE can also be expressed as

$$E = \frac{1}{2}(u'^2 + v'^2 + w'^2). \tag{2}$$

These fluctuation components can be obtained by subtracting the average of the observed wind speed data within a time window of duration N. In the subsequent estimation of the turbulent energy

dissipation rate, the value of N needs to meet the requirements of the fast Fourier transform (FFT) method. In discrete FFT, 2^m data points are required, where m is an integer. Therefore, in this paper, we conducted FFT calculations for $2^8 \times 5$ s points (i.e., approximately $N \approx 20$ min) using the data obtained from the wind lidar. All budget terms use the same duration window N. For the ultrasonic anemometer, $2^{14} \times 0.1$ s points (i.e., approximately 27 min) are required. Due to the spatial resolution of the wind lidar data being 30 m, the TKE at a height of 150 m was selected from the vertical profile obtained by wind lidar (shown in orange) and compared with the results obtained by the three-dimensional ultrasonic anemometer at a height of 160 m (shown in blue) on the tower from October 1 to 9, 2022, as shown in Figure 3(a). From the figure, it can be seen that the two data sets have a very high degree of consistency, with a correlation coefficient of 0.98. By taking the time derivative of TKE($\Delta t \approx 5$ s), a comparison of the tendency term obtained with both sets of instruments is obtained, as shown in Figure 3(b). It can be seen from this plot that the wind lidar data can reflect the trend of turbulence changes very well, with a correlation coefficient of 0.97.
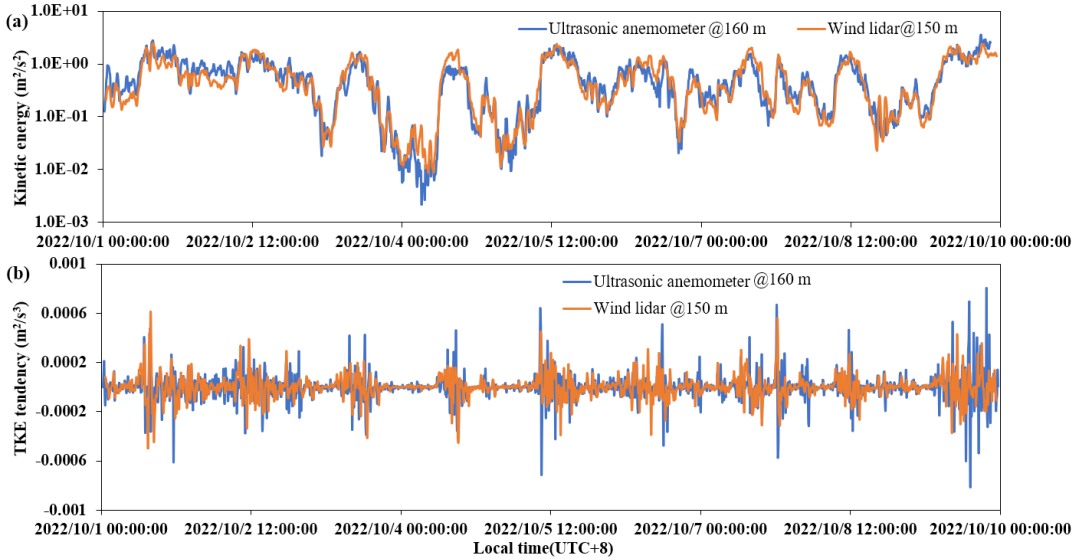
Figure 3. Comparison of TKE (a) and tendency term (b) obtained with the ultrasonic anemometer (blue) and wind lidar (orange).

3.3 Determination of the Dissipation Rate

Calculation of the dissipation rate is a major challenge. In our previous work, we proposed a method based on wind lidar to detect atmospheric turbulent energy directly (Xian et al., 2024c; Xian et al., 2024b). In the current study, we directly obtain the dissipation rate based on this foundation. According to Kolmogorov's theory of a local homogeneous and isotropic medium (Kolmogorov, 1941), the turbulence spectrum can be represented as

$$P(k) = c\varepsilon^{2/3}k^n, \tag{2}$$

$$k = \frac{2\pi f}{U}, \tag{3}$$

where the units of P are m^3/s^2, c is the Kolmogorov constant (0.55), ε is the turbulent kinetic dissipation rate (m^2/s^3), n is the power-law exponent, f is the frequency (1/s), k is the wave number (1/m), and U is the average wind speed (m/s). The turbulence spectrum P is obtained by performing fast Fourier transform on data with a time window of 20 min. In the case of a known spectrum, the dissipation rate can be obtained by the following formula

$$\varepsilon = \{\frac{P(k_1) - P(k_0)}{c(k_1^{\,n} - k_0^{\,n})}\}^{3/2} \quad . \tag{4}$$

In our previous work, we demonstrated that wind lidar can reflect the spectral characteristics of TKE in the range of f from $10^{-2.5}$ to 10^{-1} Hz; therefore, in this study these two values are used for k_0 and k_1, respectively (Xian et al., 2024c). In most weather conditions (e.g. sunny or cloudy), the turbulence spectrum estimated by wind lidar is capable of extending into the inertial subrange; however, in some cases this is not possible, which results in statistical errors (Xian et al., 2024c). This is mainly due to the detection frequency of wind lidar being only 0.2 Hz. According to Kolmogorov's theory of local isotropic turbulence, the value of n is –5/3, which is also known as the "–5/3 power law." In a previous study, we revealed that the distribution of the power-law exponent in the vertical direction of the boundary layer varies between –5/3 and –1. Thus, at the top of the boundary layer, the assumption of local homogeneity and isotropy is not satisfied (Xian et al., 2024c). Therefore, when calculating the dissipation rate, we consider n as a variable and obtain it by linearly fitting the turbulence spectrum in logarithmic coordinates (Xian et al., 2024c), which is then substituted into Equation (4) to obtain the dissipation rate. Figure 4 shows a comparison of TKE dissipation rates obtained with the three-dimensional ultrasonic anemometer (shown in blue) and the wind lidar (shown in orange) from October 1 to 9, 2022. It can be seen that the two data sets have high consistency, with a correlation coefficient of 0.96.
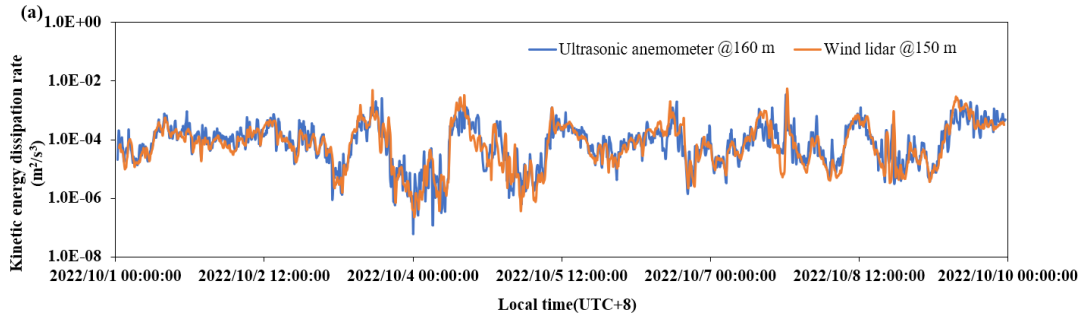
Figure 4. Comparison of the TKE dissipation rate obtained with the ultrasonic anemometer (blue) and wind lidar (orange).

3.4 Determination of the Shear Generation Term

Shear generation is a key term in the turbulent energy budget, representing the generation of turbulent energy due to the vertical shear of the wind (i.e., the variation of wind speed with height). This term is calculated by multiplying the turbulent shear stress, $u'w'$ ($v'w'$), by the wind speed gradient. In this study, the shear generation term of the wind lidar is calculated by the following steps.

(1) *Calculate the turbulent shear stress*. The shear generation term is the product of turbulent fluctuations along the wind direction and vertical wind speed components, i.e. $u'w'$ and $v'w'$.

(2) *Calculate the shear generation term*. This is done using the following equation

$$S = -\overline{u'w'}\frac{\Delta u}{\Delta z} - \overline{v'w'}\frac{\Delta v}{\Delta z}. \qquad (5)$$

For wind lidar, due to its spatial resolution of 30 m, Δz = 30 m. For the ultrasonic anemometer, Δz = 160 m. By calculating the shear generation terms for different height layers, the shear generation terms for the entire boundary layer are obtained. Due to Δz = 160 m, the shear generation term obtained by the ultrasonic anemometer has a relatively large error. Therefore, we compared the $u'w'$ and $v'w'$ obtained by the wind lidar and ultrasonic anemometer.

Figure 5 shows a comparison of the turbulent shear stresses, $u'w'$ and $v'w'$, estimated by the ultrasonic anemometer (in blue) and the wind lidar instrument (in orange) from October 1 to 9, 2022. It can be seen from this figure that the wind lidar can reflect the trend of turbulent shear stress very accurately. In addition, we can also see that there are multiple positive peaks in the momentum flux detected by the ultrasonic anemometer, but the wind lidar did not observe the same phenomenon at the corresponding time. It is speculated that one of the reasons is that the spatial resolution of the wind lidar is 30 m, which means that its results are the average effect within these 30 m, equivalent to smoothing the data, resulting in a difference in peak size between the two. Another possibility is that ultrasonic anemometers have a higher monitoring frequency (10 Hz), compared to the wind lidar's 0.2 Hz, which can detect faster changes in high-frequency energy.
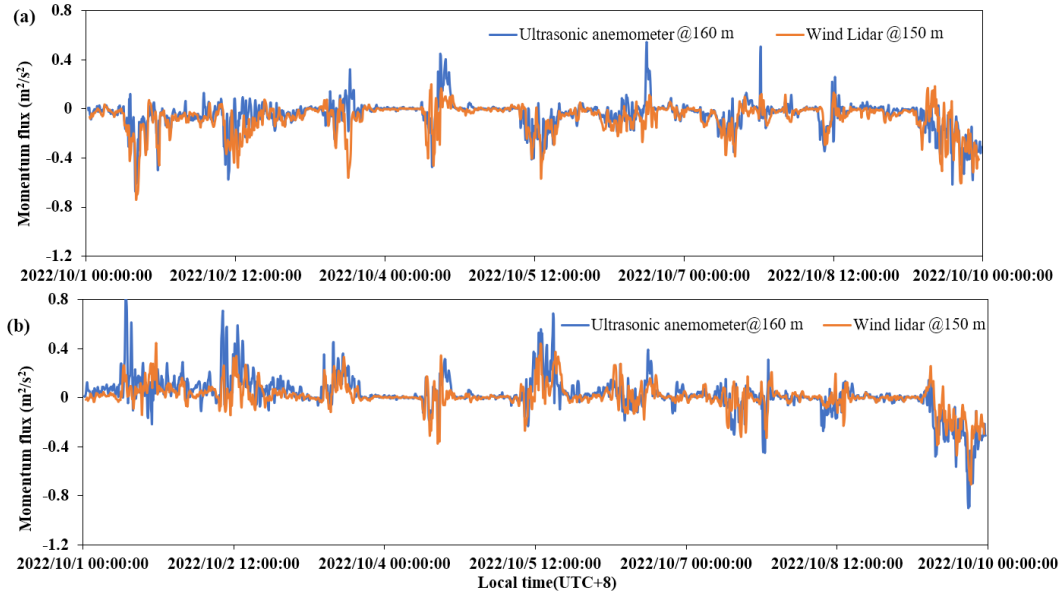
Figure 5. Comparison of the turbulent shear stresses, $u'w'$ and $v'w'$, obtained with the ultrasonic anemometer (blue) and wind lidar (orange).

3.5 Determination of the Turbulent Transport Term

The turbulent transport term is calculated by calculating the vertical derivative of the product of the turbulent velocity component in the vertical direction and TKE, as shown in the formula

$$T_t = -\frac{\partial \overline{w'E'}}{\partial z} = -\frac{1}{2}\frac{\Delta(\overline{w'u'^2} + \overline{w'v'^2} + \overline{w'w'^2})}{\Delta z}. \qquad (6)$$

As can be seen, it is necessary to calculate the third-order moments of the vertical and horizontal wind speed components for each altitude layer, namely $w'u'^2$, $w'v'^2$, and $w'w'^2$. Furthermore, the turbulent transport term can be estimated by taking the spatial derivatives of the aforementioned third-order moments. For the wind lidar, due to its spatial resolution of 30 m, $\Delta z = 30$ m. For comparison, we performed spatial differentiation on the data obtained with the ultrasonic anemometer at 160 m and 320 m to obtain a slightly rough transmission term, which was compared with the turbulent transmission term obtained from the wind lidar, as shown in Figure 6. From the graph, it can be seen that although there is a distance of 160 m between the two ultrasonic anemometers (shown in blue), the results obtained are still consistent with those of the wind lidar (shown in orange), with a correlation coefficient of 0.91, which to some extent indicates that the wind lidar can reflect the trend of the turbulence transport term.
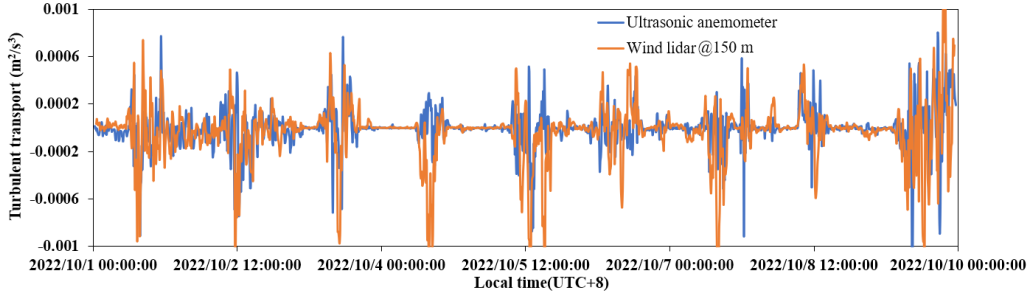
Figure 6. Comparison of turbulent transport terms obtained with the ultrasonic anemometer (blue) and wind lidar (orange).

3.6 Determination of the Pressure Transport Term

Static pressure fluctuations in the atmosphere are very small (0.01–0.05 hPa), and hence, are extremely difficult to measure, and there is little understanding of this term currently. Previous studies have attempted to use microbarometers and vertical displacement sonar anemometers to calculate the pressure velocity covariance, but the results obtained were very scattered and did not show a clear trend towards stationarity (Pozzobon et al., 2023; Acevedo et al., 2016). In practical applications, researchers have used other methods to address this challenge. In some cases, the pressure transport term is estimated through residual calculations, which indicate that it negligible in practical operations (Kaimal and Finnigan, 1994; Wyngaard, 2010; Pozzobon et al., 2023); therefore, it is ignored in this study.

3.7 Determination of the Buoyancy Generation Term

From the composition of the buoyancy generation term, it can be seen the calculation of B requires high-resolution temperature profile data. However, at present, due to the lack of vertical detection methods with high spatial and temporal resolution for temperature, vertical structural detection of buoyancy generation terms remains a major technical challenge. Therefore, in this study, we obtain the B term indirectly. After obtaining each budget term earlier, the buoyancy generation term was obtained through the residual method, i.e.,

$$B = E_t - S - T_t + D. \tag{7}$$

The accuracy and reliability of the B term will be directly affected by the reliability and accuracy of the calculated results of the other terms. Due to the ability of wind lidar to obtain accurate three-dimensional wind speeds, the terms E_t, S, D, and T_t are accurately obtained in turn. Therefore, the error

mainly comes from the assumption that the pressure transport term, T_p, is negligible. We will test this assumption in Section 4.

4 Results and Discussion

Based on the proposed method, we obtained the distribution of the buoyancy generation term at
310 different heights/layers within the boundary layer. According to the equation for the buoyancy generation term, the data from the three-dimensional ultrasonic anemometer and thermometer can be inserted into it to obtain the buoyancy generation terms for the two altitude layers for which the data were obtained.

A comparison of the lidar data obtained at 150 m and 330 m with the ultrasonic anemometer data measured at 160 m and 320 m is shown in Figure 7. From the figure, it can be seen that there is a high
315 degree of consistency between the two altitude levels, which preliminarily verifies that the wind lidar instrument can achieve vertical monitoring of the buoyancy generation term. Furthermore, the buoyancy generation term (B') estimated from the three-dimensional ultrasonic anemometer data was used as the standard value. The error ($\Delta B = B - B'$) of the buoyancy generation term (B) detected by the wind lidar was calculated, and its distribution was statistically analyzed, as shown in Figures 8(a) and (b). From this
320 error distribution, it can be inferred that the average error is very close to 0, indicating that the proposed method does not have significant systematic errors. According to the statistical results, at a height of 160 m, the average absolute error is less than 0.00013 m^2/s^3; at 320 m, the average absolute error is less than 0.00014 m^2/s^3. After using the 3σ method to remove abnormal data, correlation graphs of the buoyancy generation term obtained from the three-dimensional ultrasonic anemometer and wind lidar data were
325 plotted, as shown in Figure 8(c) and (d), respectively. From the plot, it can be seen that the correlation between the two data sets is greater than 0.9 at both heights, indicating that the wind lidar data have very high reliability.
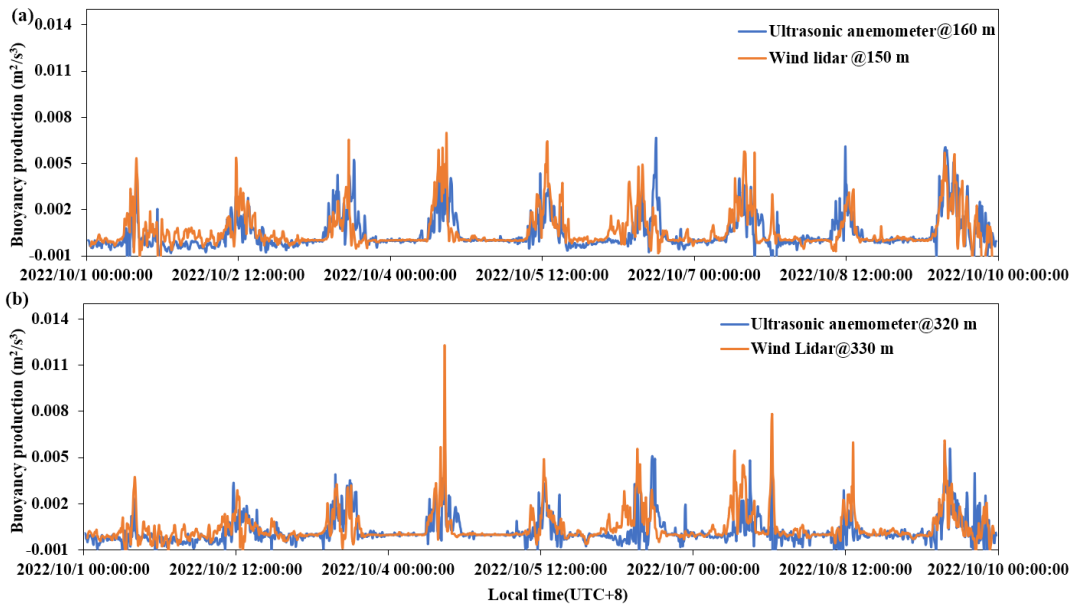
Figure 7. Comparison of buoyancy generation terms obtained with the ultrasonic anemometer (blue) and wind lidar
330 (orange).
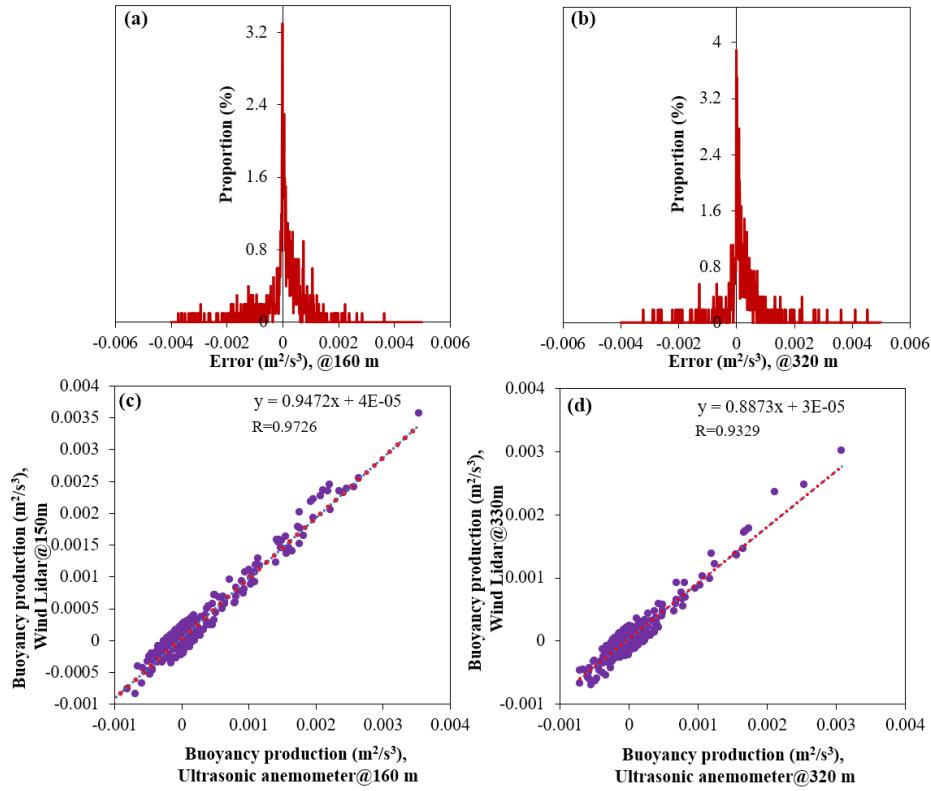
Figure 8. Error distribution of buoyancy generation term obtained by wind lidar at heights of 160 m (a) and of 320 m (b); Correlation of buoyancy generation terms obtained from ultrasonic anemometer and wind lidar at heights of 160 m (c) and of 320 m (d).

335   Through the previous series of comparisons, it was verified that the method proposed in this study can effectively detect the various budget terms of TKE. To observe the vertical structural changes of each budget term, we further selected several examples of different weather conditions for analysis, namely a cloudy and light rainy day, a sunny day with cumulus clouds, and a sunny day with low-level jets at night.

340   Figure 9 presents the spatiotemporal distribution of horizontal wind speed (a), vertical wind speed (b), TKE (c), tendency term (d), turbulent transport term (e), dissipation rate (f), shear generation term (g), and buoyancy generation term (h) on October 1, 2022. It should be noted that the color scale range of the panels varies for different TKE budget items, but for the same TKE budget item, the color scale range remains unchanged. The weather on that day consisted of low clouds with light rain (0.1 mm) around 17:00. The lowest temperature was 26°C and the highest temperature was 29°C. From the

345 horizontal wind speeds shown in Figure 9(a), it can be seen that there were low-level jets throughout the day, with wind speeds ranging from 10–15 m/s at an altitude of approximately 700 m. During the period from 00:00 to 08:00 local time, it can be seen from Figure 9(g) that the shear generation term caused by the horizontal wind had a relatively large value. However, due to the negative buoyancy generation term

350 (as shown in Figure 9(h)), it did not have an increasing effect on the turbulence overall. Therefore, the results during this period correspond to the phenomenon of weak TKE from 00:00 to 08:00 (Figure 9(c)). From 08:00 to 12:00, the ground was affected by the increase in daytime solar radiation, and the buoyancy generation term started to become positive, playing a role in generating TKE. Combined with the shear generation term generated by low-level jets, the TKE reached its maximum throughout the day

355 during this period, as shown in Figure 9(c). From 12:00 to 19:00, due to the cover of low clouds, there

was less ground radiation, and the buoyancy generation term was basically negative, which mainly suppressed and dissipated turbulence. However, the shear generation term caused by the still existing low-level jets had a relatively large value, occupying the main guiding role in the generation and maintenance of turbulent energy, resulting in strong TKE. After 19:00, although the shear generation term remained relatively large, the dissipation effect of the buoyancy generation term also increased, leading to a weakening of TKE.

Figure 10 shows the vertical distribution profiles of each budget term during the day (13:00) and at night (22:00). From Figure 10(a), it can be seen that below 400 m, the turbulent transport term was generally positive, consistent with the positive turbulent transport term observed by Nilsson et al. (2016a) under cloud cover. The difference is that our method can intuitively reveal the variation of the entire turbulent transport term with height; for example, in the height range of 400 m to 1000 m, it was about zero. From Figure 10(b), it can be seen that below 800 m, the dissipation rate was relatively small, and the buoyancy generation term was mainly negative, corresponding to a positive shear generation term, which was slightly greater than the buoyancy generation term. Therefore, turbulence was still increasing, corresponding to the TKE in Figure 9(c) still being active at night. Unlike previous tower-based observations (Nilsson et al., 2016a), we can accurately determine the height range where the buoyancy generation term is negative. For example, in Figure 10(b), the area where the buoyancy generation term is negative is below 780 m. From this example, we can see that the method proposed in this study can effectively reflect the dissipation effect of buoyancy generation on TKE under low cloud and light rain conditions.
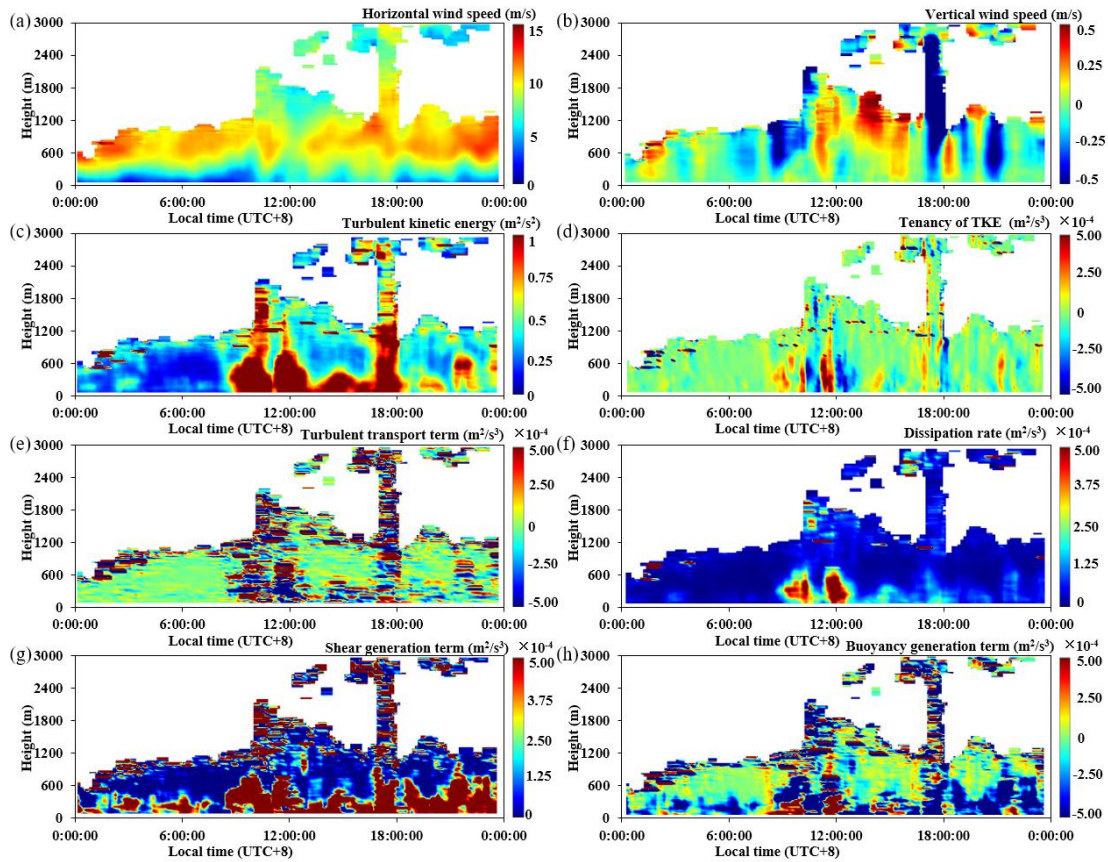
Figure 9. Temporal and spatial distributions of the horizontal wind speed (a), vertical wind speed (b), TKE (c), tendency term (d), turbulent transport term (e), dissipation rate (f), shear generation term (g), and buoyancy generation term (h) on October 1, 2022 (a cloudy and light rain day).
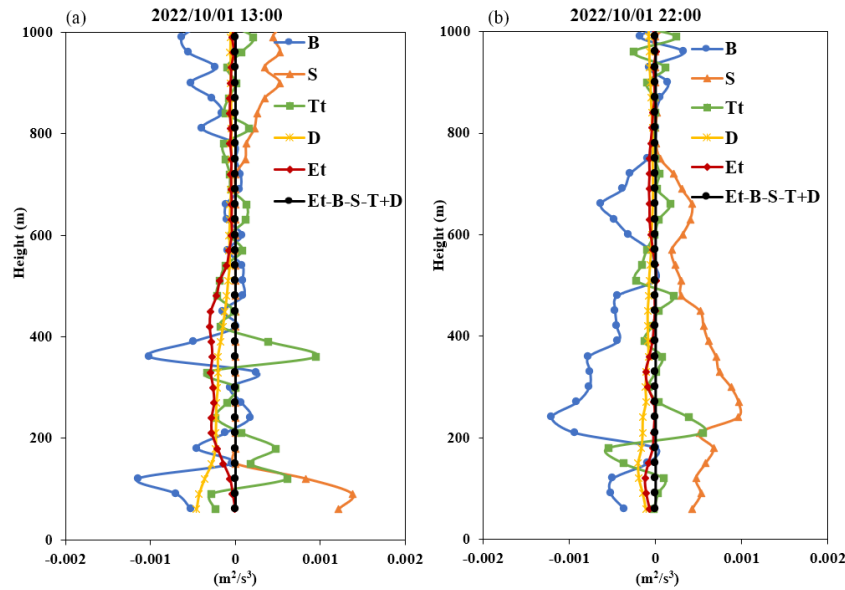
Figure 10. Vertical distribution profile of the budget terms for daytime (13:00) and nighttime (22:00) on October 1, 2022.

Figure 11 shows the spatiotemporal distributions of the horizontal wind speed (a), vertical wind speed (b), TKE (c), tendency term (d), turbulent transport term (e), dissipation rate (f), shear generation term (g), and buoyancy generation term (h) on October 5, 2022. The day was sunny with cumulus clouds, with a minimum temperature of 27°C and a maximum temperature of 32°C. From Figures 11 (f), (g), and (h), it can be seen that from 00:00 to 08:00, the shear and buoyancy generation terms were basically zero, and the dissipation rate was relatively small, which had no effect on the generation and dissipation of turbulence, corresponding to the weaker TKE seen in Figure 11(c). From 08:00 to 18:00, the shear and buoyancy generation terms were generally positive during the day. But the value of the buoyancy generation term was larger than that of the shear generation term, reaching a maximum of 1.8 km in the vertical direction, and playing a dominant role in the generation and maintenance of turbulent energy throughout the boundary layer. After 18:00, the buoyancy generation term and shear generation term were basically zero, corresponding to the weaker TKE shown in Figure 11(f).

Figure 12 shows the vertical distribution profile of each budget term during the day (13:00) and at night (22:00). From Figure 12(a), it can be seen that turbulent transport was the main dissipation term, which means that the turbulence generated near the surface was transported to the surrounding environment and the upper part of the boundary layer. Buoyancy was the main generation term, which was approximately one order of magnitude larger than the turbulent transport term. Therefore, turbulence was generally increasing, consistent with the situation where the buoyancy generation term was dominant in sunny convective conditions. From Figure 12(b), it can be seen that the buoyancy generation term was mainly negative, and the shear generation term was positive, both of which were of equal magnitude, reflecting the suppression of nighttime turbulence. In this example, we can see that the turbulent transport term during a clear and cloudless daytime could have a dissipative effect on TKE.
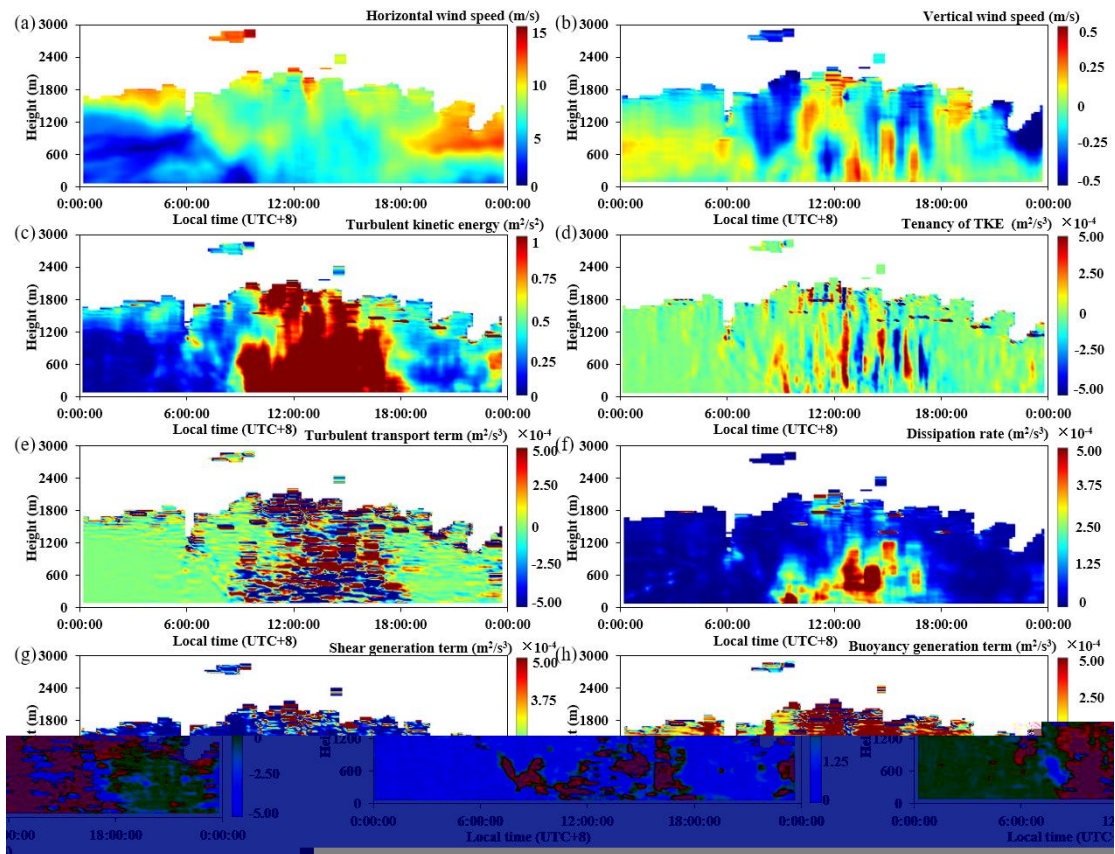
Figure 11. Temporal and spatial distributions of the horizontal wind speed (a), vertical wind speed (b), TKE (c), tendency term (d), turbulent transport term (e), dissipation rate (f), shear generation term (g), and buoyancy generation term (h) on October 5, 2022 (a sunny day with cumulus clouds).
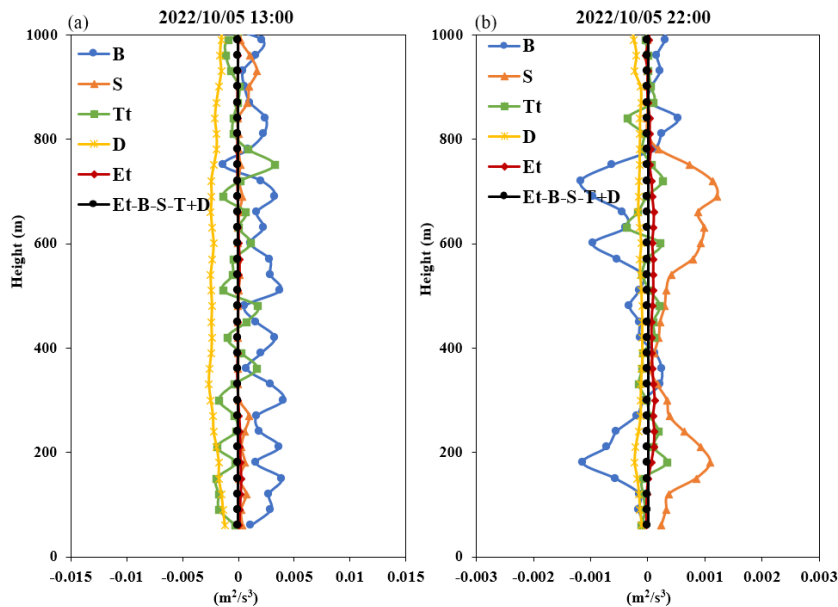
Figure 12. Vertical distribution profile of the budget terms for the daytime (13:00) and nighttime (22:00) on October 5, 2022.

Figure 13 shows the spatiotemporal distributions of the horizontal wind speed (a), vertical wind speed (b), TKE (c), tendency term (d), turbulent transport term (e), dissipation rate (f), shear generation

term (g), and buoyancy generation term (h) on October 9, 2022. The weather on that day was sunny, with a minimum temperature of 22°C and a maximum temperature of 30°C. At 08:00, the wind speed was relatively small, and due to the fact that the buoyancy generation term was basically zero before sunrise (as shown in Figure 13(h)), the TKE was relatively small, and the turbulence was relatively weak during this period, as shown in Figure 13(c). At 08:18, the ground became heated by solar radiation, and the buoyancy generation term was positive, which developed vertically to about 1 km, generating and maintaining turbulence. Corresponding to this period in Figure 13(c), the TKE was the highest throughout the day. After 18:00, the buoyancy generation term became negative, suppressing the generation and maintenance of turbulence. However, at the same time, low-level jets began to appear, with maximum wind speeds greater than 15 m/s, generating a larger shear generation term that offset the inhibitory effect of the buoyancy generation term and strengthened turbulent motion. Corresponding to Figure 13(c), it can be seen that the value of TKE was still relatively large during this period.

Figure 14 shows the vertical distribution profile of each budget term during the day (13:00) and at night (22:00). From Figure 14(a), it can be seen that the shear generation term was about zero, with the dissipation rate and turbulence transport being the main dissipation terms, and buoyancy being the main generation term; the latter's magnitude was about twice that of the turbulence transport term, so turbulence always intensified. From Figure 14(b), it can be seen that the buoyancy generation term and turbulent transport term exhibited similar magnitudes, which basically cancelled each other out at both heights. In addition, shear was the main generation term, which caused the turbulence, and hence turbulent energy, to increase, as shown in Figure 13 (c). From this example, we can see that, by using the method proposed in this study, we have determined that the main dissipation effect during a clear and cloudless day primarily comes from the dissipation rate term, while the shear generation term under low-level jets enhances the turbulent energy, during clear and days and nights.

In summary, from the individual cases of different weather conditions mentioned above, we can see that during the day, turbulent transport and the dissipation rate are the main dissipation terms, while buoyancy generation is the main dissipation term at night. In addition, with the proposed method we are able to monitor the vertical distribution of various budget terms within the boundary layer, and can comprehensively reflect the impact of each budget term on the vertical structure of turbulent energy.
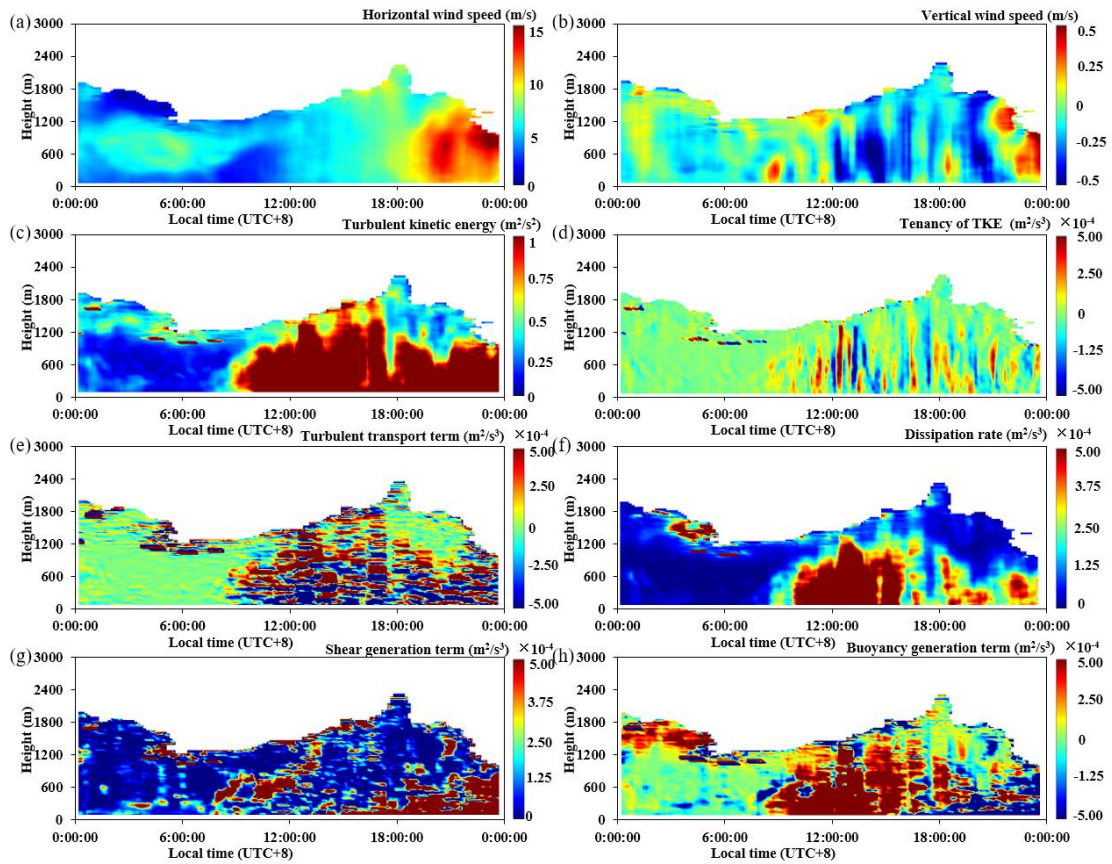
Figure 13. Temporal and spatial distributions of the horizontal wind speed (a), vertical wind speed (b), TKE (c), tendency term (d), turbulent transport term (e), dissipation rate (f), shear generation term (g), and buoyancy generation term (h) on October 9, 2022 (a sunny day with low-level jets at night).
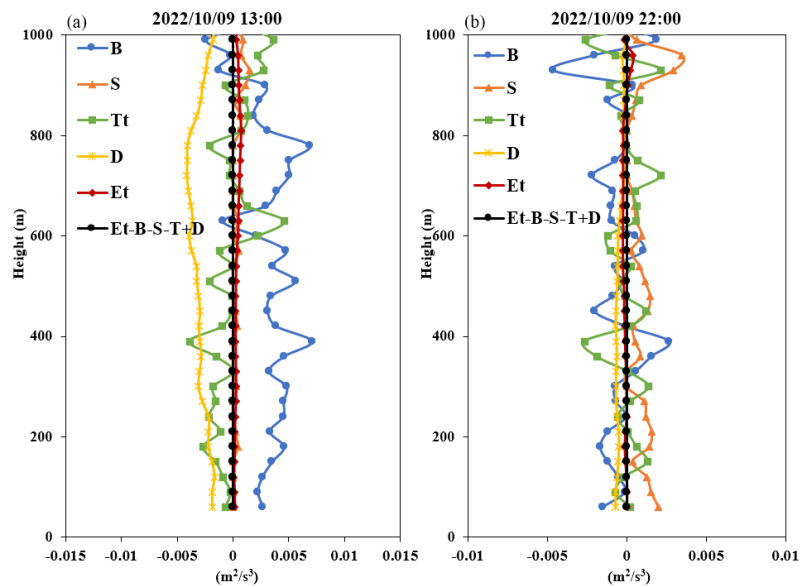
Figure 14. Vertical distribution profile of the budget terms for daytime (13:00) and nighttime (22:00) on October 9, 2022.

Conclusion

We proposed a new method for detecting turbulent energy budget terms based on coherent wind lidar, and through strict data quality control, ensured the accuracy and reliability of the obtained data. By

comparing these data with those obtained with a three-dimensional ultrasonic anemometer, the results indicate that the error of the buoyancy generation term detected by the proposed method is relatively small, with an average absolute value of less than 0.00014 m^2/s^3, which verify the accuracy and reliability of our method. Based on the detection principle of wind lidar, the method proposed in this study is applicable during sunny and cloudy conditions; however, it is not suitable for deployment during periods of heavy rainfall. Furthermore, this method holds potential for elucidating turbulence convection interactions and convective initiation before precipitation occurs. It is imperative to acknowledge that due to the inability to measure pressure transport terms and monitor high-frequency turbulent energy, the error of the proposed method may increase in weather processes dominated by these two factors. This study explored the generation and dissipation mechanisms of turbulence under different weather conditions, and analyzed the effects of shear generation, buoyancy generation, turbulence transport, and dissipation rate on turbulent motion for different periods throughout the day and night. The results indicate that the buoyancy generation term plays a dissipative role in TKE under low cloud and light rain conditions. During the day, turbulent transport and the dissipation rate are the main dissipation terms, while buoyancy generation is the main dissipation term at night. The results show that the proposed method can accurately capture key parameters such as TKE, dissipation rate, shear generation, turbulent transport, and buoyancy generation, and accurately describe the spatiotemporal distribution characteristics of each budget term of turbulent energy. These research results not only provide new a perspective and method for studies of atmospheric turbulence, but can also be further applied to a wider range of meteorological research topics and practical applications, especially those related to fine observations of the vertical structure and dynamics of turbulence.

Data availability

The wind field data measured by ultrasonic anemometer can be downloaded from the Shenzhen Data Open Platform (https://opendata.sz.gov.cn/data/dataSet/toDataDetails/29200_00900273). Data to generate the figures of this paper are available at https://doi.org/10.5281/zenodo.13624484 (Xian et al., 2024a).

Author contributions

Conceptualization: J.X. and H.Y.; methodology: J.X. and N.Z.; software: J.X.; validation: Y.H. and Z. Q.; formal analysis: J.X. and N.Z.; investigation: H.Y and Z. Q.; resources: C.L. and H. L.; data curation: Y.Y. and H. L.; writing—original draft preparation: J.X.; writing—review and editing: H.Y. and N.Z.; visualization: X.L.; supervision: H.Y. and N.Z.; project administration: H.Y. and N.Z.; and funding acquisition: H.Y. and N.Z.

Competing interests

The contact author has declared that none of the authors has any competing interests.

Acknowledgements

We thank Shenzhen Darsunlaser Technology Co., Ltd. and Xinlin Yang.

Financial support

This work was supported by the Special Project for Sustainable Development of Shenzhen (KCXFZ20201221173412035), the National Natural Science Foundation of China (NSFC; U2342221 and 42275065), Key Innovation Team of China Meteorological Administration (CMA2024ZD04), Guangdong Province Science and Technology Department Project (2021B1212050024), Scientific research projects of Guangdong Provincial Meteorological Bureau (GRMC2020M29), Science and Technology Innovation Team Plan of Guangdong Meteorological Bureau (GRM-CTD202003), Open Fund for the Key Open Laboratory of Urban Meteorology of the China Meteorological Administration (LUM-2024-03), and China Postdoctoral Science Foundation (2024M751378).

References

Acevedo, O. C., Mahrt, L., Puhales, F. S., Costa, F. D., Medeiros, L. E., and Degrazia, G. A.: Contrasting structures between the decoupled and coupled states of the stable boundary layer, Quarterly Journal of the Royal Meteorological Society, 142, 693-702, 10.1002/qj.2693, 2016.

Baas, P., van de Wiel, B. J. H., van der Linden, S. J. A., and Bosveld, F. C.: From Near-Neutral to Strongly Stratified: Adequately Modelling the Clear-Sky Nocturnal Boundary Layer at Cabauw, Boundary-Layer Meteorology, 166, 217-238, 10.1007/s10546-017-0304-8, 2018.

Babic, K. and Rotach, M. W.: Turbulence kinetic energy budget in the stable boundary layer over a heterogeneous surface, Quarterly Journal of the Royal Meteorological Society, 144, 1045-1062, 10.1002/qj.3274, 2018.

Banakh, V. A., Smalikho, I. N., Falits, A. V., and Sherstobitov, A. M.: Estimating the Parameters of Wind Turbulence from Spectra of Radial Velocity Measured by a Pulsed Doppler Lidar, Remote sensing, 13, 2071, 2021.

Banakh, V. a. S., I: Coherent Doppler Wind Lidars in a Turbulent Atmosphere, Artech House Publishers, Boston, London2013.

Barman, N., Borgohain, A., Kundu, S. S., Roy, R., Saha, B., Solanki, R., Kumar, N. V. P. K., and Raju, P. L. N.: Daytime Temporal Variation of Surface-Layer Parameters and Turbulence Kinetic Energy Budget in Topographically Complex Terrain Around Umiam, India, Boundary-Layer Meteorology, 172, 149-166, 10.1007/s10546-019-00443-6, 2019.

Bodini, N., Lundquist, J. K., and Newsom, R. K.: Estimation of turbulence dissipation rate and its variability from sonic anemometer and wind Doppler lidar during the XPIA field campaign, Atmospheric Measurement Techniques, 11, 4291-4308, 10.5194/amt-11-4291-2018, 2018.

Byzova, N. L., Ivanov, V. N., and Garger, E. K.: Turbulence in Atmospheric Boundary Layer, Gidrometeoizdat, Leningrad1989.

525 Canut, G., Couvreux, F., Lothon, M., Legain, D., Piguet, B., Lampert, A., Maurel, W., and Moulin, E.: Turbulence fluxes and variances measured with a sonic anemometer mounted on a tethered balloon, Atmospheric Measurement Techniques, 9, 4375-4386, 10.5194/amt-9-4375-2016, 2016.

Caughey, S. J. and Wyngaard, J. C.: Turbulence kinetic-energy budget in convective conditions, Quarterly Journal of the Royal Meteorological Society, 105, 231-239, 1979.

530 Elguernaoui, O., Reuder, J., Li, D., Maronga, B., Paskyabi, M. B., Wolf, T., and Esau, I.: The Departure from Mixed-Layer Similarity During the Afternoon Decay of Turbulence in the Free-Convective Boundary Layer: Results from Large-Eddy Simulations, Boundary-Layer Meteorology, 10.1007/s10546-023-00812-2, 2023.

Goger, B., Rotach, M. W., Gohm, A., Fuhrer, O., Stiperski, I., and Holtslag, A. A. M.: The Impact of
535 Three-Dimensional Effects on the Simulation of Turbulence Kinetic Energy in a Major Alpine Valley, Boundary-Layer Meteorology 168, 1-27, 10.1007/s10546-018-0341-y, 2018.

Guo, J., Zhang, J., Yang, K., Liao, H., Zhang, S., Huang, K., Lv, Y., Shao, J., Yu, T., Tong, B., Li, J., Su, T., Yim, S. H. L., Stoffelen, A., Zhai, P., and Xu, X.: Investigation of near-global daytime boundary layer height using high-resolution radiosondes: first results and comparison with ERA5, MERRA-2,
540 JRA-55, and NCEP-2 reanalyses, Atmos. Chem. Phys., 21, 17079-17097, 10.5194/acp-21-17079-2021, 2021.

Hang, C., Nadeau, D. F., Pardyjak, E. R., and Parlange, M. B.: A comparison of near-surface potential temperature variance budgets for unstable atmospheric flows with contrasting vegetation cover flat surfaces and a gentle slope, Environmental Fluid Mechanics, 20, 1251-1279, 10.1007/s10652-018-9647-
545 z, 2020.

Hariprasad, K., Srinivas, C. V., Singh, A. B., Rao, S. V. B., Baskaran, R., and Venkatraman, B.: Numerical simulation and intercomparison of boundary layer structure with different PBL schemes in WRF using experimental observations at a tropical site, Atmospheric Research, 145, 27-44, 10.1016/j.atmosres.2014.03.023, 2014.

550 Heilman, W. E., Clements, C. B., Zhong, S., Clark, K. L., and Bian, X.: Atmospheric Turbulence, in: Encyclopedia of Wildfires and Wildland-Urban Interface (WUI) Fires, edited by: Manzello, S. L., Springer International Publishing, Cham, 1-17, 10.1007/978-3-319-51727-8_137-1, 2018.

Hong, S.-Y., Noh, Y., and Dudhia, J.: A new vertical diffusion package with an explicit treatment of entrainment processes, Monthly Weather Review, 134, 2318-2341, 10.1175/MWR3199.1, 2006.

555 Janjic, Z. I.: The Step-Mountain Eta Coordinate Model - Further Developments of The Convection, Viscous Sublayer, And Turbulence Closure Schemes, Monthly Weather Review, 122, 927-945, 10.1175/1520-0493(1994)122<0927:TSMECM>2.0.CO;2, 1994.

Jensen, D. D., Price, T. A., Nadeau, D. F., Kingston, J., and Pardyjak, E. R.: Coastal Wind and Turbulence Observations during the Morning and Evening Transitions over Tropical Terrain, Journal of
560 Applied Meteorology and Climatology, 56, 3167-3185, 10.1175/JAMC-D-17-0077.1, 2017.

Kaimal, J. C. and Finnigan, J. J.: Atmospheric boundary layer flows, Atmospheric boundary layer flows :1994.

Kaimal, J. C., Wyngaard, J. C., Haugen, D. A., Cote, O. R., Izumi, Y., Caughey, S. J., and Readings, C. J.: Turbulence Structure in Convective Boundary-Layer, Journal of the atmospheric sciences, 33, 2152-2169, 10.1175/1520-0469(1976)033<2152:TSITCB>2.0.CO;2, 1976.

Kolmogorov, A. N.: Energy dissipation in locally isotropic turbulence, Dokl. Akad. Nauk SSSR, 32, 19-21, 1941.

Li, J., Dou, J. X., Lenschow, D. H., Zhou, M. Y., Meng, L. H., Qiu, X. B., Pan, Y. B., and Zhang, J. J.: Analysis of Boundary Layer Structure, Turbulence, and Flux Variations before and after the Passage of a Sea Breeze Front Using Meteorological Tower Data, Journal of Meteorological Research, 37, 855-877, 10.1007/s13351-023-3057-y, 2023.

Lobocki, L.: Turbulent Mechanical Energy Budget in Stably Stratified Baroclinic Flows over Sloping Terrain, Boundary-Layer Meteorology, 164, 353-365, 10.1007/s10546-017-0251-4, 2017.

Massman, W.: Handbook of Micrometeorology: A Guide for Surface Flux Measurement and Analysis, Kluwer Academic, Boston2006.

Nilsson, E., Lohou, F., Lothon, M., Pardyjak, E., Mahrt, L., and Darbieu, C.: Turbulence kinetic energy budget during the afternoon transition - Part 1: Observed surface TKE budget and boundary layer description for 10 intensive observation period days, Atmospheric Chemistry and Physics, 16, 8849-8872, 10.5194/acp-16-8849-2016, 2016a.

Nilsson, E., Lothon, M., Lohou, F., Pardyjak, E., Hartogensis, O., and Darbieu, C.: Turbulence kinetic energy budget during the afternoon transition - Part 2: A simple TKE model, Atmospheric Chemistry and Physics, 16, 8873-8898, 10.5194/acp-16-8873-2016, 2016b.

Pozzobon, A. E. D., Acevedo, O. C., Puhales, F. S., Oliveira, P. E. S., Maroneze, R., and Costa, F. D.: Observed Budgets of Turbulence Kinetic Energy, Heat Flux, and Temperature Variance Under Convective and Stable Conditions, Boundary-Layer Meteorology, 187, 619-642, 10.1007/s10546-023-00788-z, 2023.

Rios, G. and Ramamurthy, P.: Turbulence in the Mixed Layer Over an Urban Area: A New York City Case Study, Boundary-Layer Meteorology, 10.1007/s10546-023-00819-9, 2023.

Solanki, R., Guo, J., Lv, Y., Zhang, J., Wu, J., Tong, B., and Li, J.: Elucidating the atmospheric boundary layer turbulence by combining UHF radar wind profiler and radiosonde measurements over urban area of Beijing, Urban Climate, 43, 101151, 2022.

Stull, R. B.: An Introduction to Boundary Layer Meteorology, Springer Netherlands1988.

Tong, B., Guo, J., Wang, Y., Li, J., Yun, Y., Solanki, R., Hu, N., Yang, H., Li, H., Su, J., He, Q., Zhou, Y., Zhang, K., and Zhang, Y.: The near-surface turbulent kinetic energy characteristics under the different convection regimes at four towers with contrasting underlying surfaces, Atmospheric Research, 270, 10.1016/j.atmosres.2022.106073, 2022.

Wyngaard, J. C.: Turbulence in the Atmosphere, Cambridge University Press, New York2010.

Xian, J., Yang, H., and Zhang, N.: Turbulent Energy Budget Analysis Based on Coherent Wind Lidar Observations [dataset], 10.5281/zenodo.13624484, 2024a.

Xian, J., Luo, H., Lu, C., Lin, X., Yang, H., and Zhang, N.: Characteristics of the atmospheric boundary layer height: A perspective on turbulent motion, Science of The Total Environment, 919, 170895, https://doi.org/10.1016/j.scitotenv.2024.170895, 2024b.

Xian, J. H., Zhang, N., Lu, C., Yang, H. L., and Qiu, Z. X.: Novel Method for Determining the Height of the Stable Boundary Layer under Low-Level Jet by Judging the Shape of the Wind Velocity Variance

605   Profile, Remote Sensing 15, 10.3390/rs15143638, 2023.

Xian, J. H., Lu, C., Lin, X. L., Yang, H. L., Zhang, N., and Zhang, L.: Directly measuring the power-law exponent and kinetic energy of atmospheric turbulence using coherent Doppler wind lidar, Atmospheric Measurement Techniques, 17, 1837-1850, 10.5194/amt-17-1837-2024, 2024c.

Xie, B., Hunt, J. C. R., Carruthers, D. J., Fung, J. C. H., and Barlow, J. F.: Structure of the planetary

610   boundary layer over Southeast England: Modeling and measurements, Journal of Geophysical Research-Atmospheres, 118, 7799-7818, 10.1002/jgrd.50621, 2013.

Yus-Diez, J., Udina, M., Rosa Soler, M., Lothon, M., Nilsson, E., Bech, J., and Sun, J.: Nocturnal boundary layer turbulence regimes analysis during the BLLAST campaign, Atmospheric Chemistry and Physics, 19, 9495-9514, 10.5194/acp-19-9495-2019, 2019.

615   Zhou, Q. J., Li, L., Chan, P. W., Cheng, X. L., Lan, C. X., Su, J. C., He, Y. Q., and Yang, H. L.: Observational Study of Wind Velocity and Structures during Supertyphoons and Convective Gales over Land Based on a 356-m-High Meteorological Gradient Tower, Journal of applied meteorology and climatology, 62, 103-118, 10.1175/JAMC-D-22-0013.1, 2023.